

# Golden single-atomic-site platinum electrocatalysts

Paul N. Duchesne<sup>1</sup>, Z. Y. Li<sup>2,9</sup>, Christopher P. Deming<sup>3,9</sup>, Victor Fung<sup>4,9</sup>, Xiaojing Zhao<sup>5</sup>, Jun Yuan<sup>6</sup>, Tom Regier<sup>7</sup>, Ali Aldabahi<sup>8</sup>, Zainab Almarhoon<sup>8</sup>, Shaowei Chen<sup>3</sup>, De-en Jiang<sup>4</sup>, Nanfeng Zheng<sup>5</sup> and Peng Zhang<sup>1\*</sup>

**Bimetallic nanoparticles with tailored structures constitute a desirable model system for catalysts, as crucial factors such as geometric and electronic effects can be readily controlled by tailoring the structure and alloy bonding of the catalytic site. Here we report a facile colloidal method to prepare a series of platinum–gold (PtAu) nanoparticles with tailored surface structures and particle diameters on the order of 7 nm. Samples with low Pt content, particularly Pt<sub>4</sub>Au<sub>96</sub>, exhibited unprecedented electrocatalytic activity for the oxidation of formic acid. A high forward current density of 3.77 A mg<sub>Pt</sub><sup>-1</sup> was observed for Pt<sub>4</sub>Au<sub>96</sub>, a value two orders of magnitude greater than those observed for core-shell structured Pt<sub>78</sub>Au<sub>22</sub> and a commercial Pt nanocatalyst. Extensive structural characterization and theoretical density functional theory simulations of the best-performing catalysts revealed densely packed single-atom Pt surface sites surrounded by Au atoms, which suggests that their superior catalytic activity and selectivity could be attributed to the unique structural and alloy-bonding properties of these single-atomic-site catalysts.**

Platinum (Pt) has a long history of use in catalysis, due primarily to its high activity in a wide range of chemical reactions<sup>1</sup>. However, it faces major obstacles in some reactions, which include the problem of carbon monoxide (CO) poisoning in the formic acid oxidation (FAO) reaction<sup>2</sup>. Due to the very strong binding affinity of CO at Pt surfaces, exposure to even small quantities of CO can gradually poison (that is, deactivate) a Pt catalyst<sup>3</sup>. In recent years, it has become common to alloy Pt with other metals to modify its catalytic properties<sup>4–7</sup>; thus, it seems reasonable that this approach could also be used to address the issue of CO poisoning and enhance the performance of such Pt catalysts<sup>8,9</sup>. Recent advances in nanoparticle synthesis have allowed the preparation of bimetallic nanocatalysts with increasingly well-defined alloy structures<sup>10–13</sup>. An important quality of these bimetallic nanoparticles is that the interaction between atoms of different metals at the nanoparticle surface can result in a significantly enhanced catalytic activity due to both geometric and electronic effects<sup>14–16</sup>. By definition, these alloy interactions occur at the boundaries between domains of the two metals; thus, any catalytic enhancement effect should also be maximized by increasing the degree of intermetallic mixing at the nanoparticle surface<sup>16</sup>. A very interesting and little-researched limit to this mixing is found in single-Pt-site catalysis in an alloy nanoparticle system, wherein distinct geometric and electronic effects set it apart from other phase-segregated surface nanostructures via the so-called ‘ensemble effect’ theory<sup>17–21</sup>.

Here we present a series of colloidal bimetallic PtAu nanoparticles, obtained via a facile solution-phase synthesis, that feature stable single-atom Pt catalytic sites with a high FAO activity.

Electrocatalytic measurements reveal a remarkable enhancement in activity that is highly dependent on the PtAu composition of the sample. The characterization of such materials is very challenging, as Pt and Au have nearly identical atomic numbers. Nonetheless, we demonstrate that convincing conclusions can be achieved through the use of several complementary techniques, which include X-ray absorption spectroscopy (XAS), X-ray photoelectron spectroscopy (XPS), energy-dispersive X-ray spectroscopy (EDX), high-angle annular dark-field scanning transmission electron microscopy (HAADF-STEM) and electrochemical measurements, with each offering its own insights into the structure of the subject material. The results of this structural characterization, together with density functional theory (DFT) modelling, demonstrate that it is not only elemental composition that dictates the electrocatalytic activity of the PtAu nanoparticles—the most critical role is played by the local bonding environment of single-atomic-site Pt surface atoms.

The bimetallic PtAu nanoparticles used in this study were prepared from stock solutions of Pt and Au chloride precursor salts using an adapted colloidal synthetic method<sup>16</sup>. This synthetic procedure and a complete set of the PtAu samples with systematically varied compositions from 4% Pt to 96% Pt are provided in Supplementary Fig. 1. An illustration of the nanoparticle formation from ions in solution is shown in Fig. 1a. Of particular importance was the replacement of the CO reducing agent/co-ligand (used in the original synthesis) with ethylene glycol, such that the PtAu nanoparticles were prepared in a CO-free environment. After the synthesis, these nanoparticles were deposited onto a carbon powder support material in preparation for catalytic activity testing.

<sup>1</sup>Department of Chemistry, Dalhousie University, Halifax, NS, Canada. <sup>2</sup>Nanoscale Physics Research Laboratory, School of Physics & Astronomy, University of Birmingham, Birmingham, UK. <sup>3</sup>Department of Chemistry and Biochemistry, University of California, Santa Cruz, CA, USA. <sup>4</sup>Department of Chemistry, University of California, Riverside, CA, USA. <sup>5</sup>State Key Laboratory for Physical Chemistry of Solid Surfaces, Collaborative Innovation Center of Chemistry for Energy Materials, and National & Local Joint Engineering Research Center for Preparation Technology of Nanomaterial, College of Chemistry and Chemical Engineering, Xiamen University, Xiamen, China. <sup>6</sup>Department of Physics, University of York, York, UK. <sup>7</sup>Canadian Light Source, Saskatoon, SK, Canada. <sup>8</sup>Department of Chemistry, College of Science, King Saud University, Riyadh, Saudi Arabia. <sup>9</sup>These authors contributed equally: Z.Y. Li, Christopher P. Deming, Victor Fung. \*e-mail: [peng.zhang@dal.ca](mailto:peng.zhang@dal.ca)

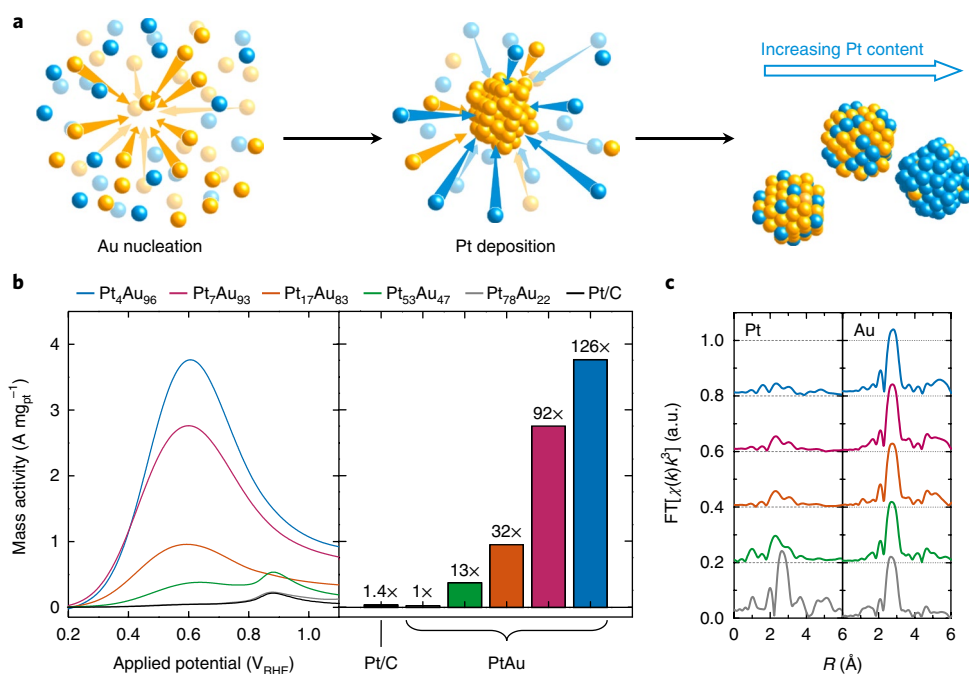


**Fig. 1 | Synthesis, reactivity and EXAFS of catalysts.** **a**, Illustration of the nanoparticle formation via the reduction of solvated ions. **b**, Pt mass-normalized anodic sweeps obtained from PtAu nanoparticle catalysts in an electrolyte that contained 0.1M concentrations of both  $\text{HClO}_4$  and  $\text{HCOOH}$ , with the peak currents graphed for comparison (left). The data acquired from a commercial Pt/C catalyst is included to provide additional context. **c**, The plotted FT-EXAFS spectra obtained from Pt and Au  $L_3$ -edge absorption spectra of PtAu nanoparticles illustrate the drastic undercoordination of Pt atoms in low-Pt-content samples, such as  $\text{Pt}_7\text{Au}_{93}$  and  $\text{Pt}_4\text{Au}_{96}$ . a.u., arbitrary units.

Transmission electron microscopy (TEM) was employed to confirm a successful sample preparation (Supplementary Fig. 2), and inductively coupled plasma optical emission spectroscopy (ICP-OES) was used to measure the relative elemental compositions and mass loadings (Supplementary Table 1). The TEM results confirmed a high degree of nanoparticle dispersion and uniformity, with observed mean particle diameters of  $\sim 7$  nm for all the samples, and ICP-OES measurements revealed an average mass loading of  $11 \pm 2$  wt% for the carbon-supported samples. The measured elemental compositions from ICP-OES (that is,  $\text{Pt}_{78}\text{Au}_{22}$ ,  $\text{Pt}_{53}\text{Au}_{47}$ ,  $\text{Pt}_{17}\text{Au}_{83}$ ,  $\text{Pt}_7\text{Au}_{93}$  and  $\text{Pt}_4\text{Au}_{96}$ ) corresponded closely to the nominal concentrations of Pt and Au used during the synthesis, and are hereafter used to distinguish between the PtAu samples.

Cyclic voltammetry (CV) analysis yielded a very interesting result as to the specific electrocatalytic activities of the PtAu nanoparticles. As can be seen from the magnitude of the Pt-mass-normalized current peaks at  $\sim 0.6 \text{ V}_{\text{RHE}}$  (RHE, reversible hydrogen electrode) in the anodic sweeps (Fig. 1b), the highest activities were observed for those samples that contained the least Pt. The most active sample,  $\text{Pt}_4\text{Au}_{96}$ , exhibited an activity greater than that of the commercial Pt/C catalyst and the least-active PtAu nanoparticle sample by up to two orders of magnitude (that is, 126 times greater than  $\text{Pt}_{78}\text{Au}_{22}$ , and 90 times greater than Pt/C). A strong correlation was observed between low FAO peak currents and the presence of a significant peak at  $\sim 0.85 \text{ V}_{\text{RHE}}$  in the CV plot. This secondary peak arises from the electrochemical oxidation of adsorbed CO molecules, which are well known to poison the surface of Pt and suppress its catalytic activity<sup>22</sup>. The absence of such a peak in the CV plots of those PtAu nanoparticles that contained the least Pt suggests that a resistance to CO poisoning may play a significant role in their enhanced catalytic activity. Note that the characterization of pure Au nanoparticles, prepared according to the same protocol, revealed no measurable activity in the FAO reaction (Supplementary Fig. 3).

To gain a structural perspective on this activity enhancement, a Fourier transform extended X-ray absorption fine structure (FT-EXAFS) analysis was performed on the PtAu nanoparticles at the Pt and Au  $L_3$  absorption edges (Fig. 1c). Detailed information regarding the local Pt and Au bonding environments in each sample was obtained by fitting these spectra (Supplementary Fig. 4), which resulted in the structural parameter values shown in Table 1. Observed trends in the coordination number and bond length values are also presented graphically in Supplementary Fig. 5. Although the scattering paths that involve Pt and Au atoms were too similar to produce separable peaks in the FT-EXAFS spectrum (Supplementary Fig. 6 gives a topographical illustration), this similarity made it possible to treat scattering from both Pt and Au as a single path (denoted Pt–M and Au–M for the Pt and Au  $L_3$  edges, respectively). Analysis of the resulting bond lengths suggests that the Pt atoms in  $\text{Pt}_7\text{Au}_{93}$  and  $\text{Pt}_4\text{Au}_{96}$ , the most highly active PtAu samples, were present almost exclusively as single-atom sites surrounded by atoms of Au. This observation is based on the close agreement between the measured Pt–M bond lengths (2.82 Å) and the expected bimetallic bond length of 2.822 Å for a homogeneous PtAu alloy, as calculated from experimental Pt–Pt and Au–Au bond lengths in pure Pt and Au nanoparticles (Supplementary Table 2). Further evidence for the single-atom structure of Pt in these two samples is provided via HAADF-STEM, electrochemistry and XPS valence band analyses. It is notable that a similar Pt–M bond distance was also observed for  $\text{Pt}_{17}\text{Au}_{83}$ ; however, its Pt–M coordination number is identical to that of the core-shell structured nanoparticles ( $\text{Pt}_{53}\text{Au}_{47}$  and  $\text{Pt}_{78}\text{Au}_{22}$ ) and considerably higher than that of the single-atom Pt samples. These results indicate that  $\text{Pt}_{17}\text{Au}_{83}$  exhibits a mixed structure that contains both single-atom and few-atom Pt cluster regions, with more of these located within the core of the nanoparticle. Additional support for this conclusion is provided by the particularly large Debye–Waller coefficient ( $\sigma^2$ ) value obtained for  $\text{Pt}_{17}\text{Au}_{83}$ , which indicates that there is greater variation among

**Table 1 | Structural parameter values for PtAu nanoparticles**

Sample	Pt-M				Au-M			
	CN (atoms)	R (Å)	$\sigma^2$ ( $10^{-3} \text{Å}^2$ )	$\Delta E_0$ (eV)	CN (atoms)	R (Å)	$\sigma^2$ ( $10^{-3} \text{Å}^2$ )	$\Delta E_0$ (eV)
Pt <sub>100</sub> Au <sub>0</sub>	11.1(5)	2.772(1)	2.1(2)	3.9(4)	-	-	-	-
Pt <sub>78</sub> Au <sub>22</sub>	9(1)	2.776(4)	2.6(6)	3(1)	12(1)	2.839(4)	4.3(6)	0(1)
Pt <sub>53</sub> Au <sub>47</sub>	9(2)	2.776(8)	3(2)	2(1)	12.1(9)	2.851(3)	4.2(4)	2.3(7)
Pt <sub>17</sub> Au <sub>83</sub>	9(1)	2.818(5)	8(1)	2.8(8)	11.6(9)	2.861(3)	3.6(4)	2.6(7)
Pt <sub>7</sub> Au <sub>93</sub>	7.4(9)	2.813(5)	6(1)	2.6(8)	12(1)	2.862(4)	3.4(5)	2(1)
Pt <sub>4</sub> Au <sub>96</sub>	5(2)	2.82(2)	4(3)	3(3)	11.0(8)	2.871(2)	3.1(3)	3.4(6)
Pt <sub>0</sub> Au <sub>100</sub>	-	-	-	-	12.0(4)	2.872(1)	3.4(2)	2.7(3)

These parameter values were obtained by fitting the respective Pt and Au L<sub>3</sub>-edge FT-EXAFS spectra of each nanoparticle sample. The numbers in parenthesis indicate the uncertainty ( $1\sigma$ ) in the last digit of the corresponding value. CN, coordination number.

the Pt–M bond lengths due to significant contributions from both the Pt–Pt and the Pt–Au bonds. Further evidence is also provided in the electrochemical and valence band studies.

EXAFS analysis of the local coordination numbers revealed that Pt atoms were undercoordinated in the PtAu nanoparticles, especially those that bear highly active single-atom sites. Coordination numbers for the Pt–M scattering path ranged from nine nearest neighbours in Pt<sub>78</sub>Au<sub>22</sub> to just five in Pt<sub>4</sub>Au<sub>96</sub>, which stands in stark contrast with the coordination number of 11 observed for pure Pt nanoparticles synthesized using the same method. Combined with Au–M coordination numbers on the order of 11–12 nearest neighbours, this evidence strongly suggests an Au-core/PtAu shell nanoparticle structure, with Pt predominantly located at surface sites. Furthermore, Pt concentrations measured using surface-sensitive XPS were consistently greater than those obtained using bulk-sensitive ICP-OES (Supplementary Fig. 7), which provides convincing evidence of Pt surface enrichment in all PtAu nanoparticle samples. The very low coordination numbers observed for Pt<sub>7</sub>Au<sub>93</sub> and Pt<sub>4</sub>Au<sub>96</sub> (seven and five, respectively) further indicate that Pt should be predominantly found on the particle surface with a high-level surface roughness that includes edge and corner sites<sup>12</sup>. X-ray absorption near-edge structure analysis of samples (Supplementary Fig. 8) further confirmed the metallic nature of both Pt and Au in these nanoparticles, and provided support for the presence of single-atom Pt sites via a positive binding-energy shift and increased white-line breadth (both indicative of increasingly isolated Pt atoms<sup>23</sup>). This high degree of direct Pt–Au interaction was also observed in the XPS data, which featured a negative shift of the Pt 4f electron binding energies of Pt<sub>17</sub>Au<sub>83</sub> and Pt<sub>4</sub>Au<sub>96</sub> (as shown in Supplementary Fig. 7). In contrast to the extensive Pt–Au mixing in those samples with a low Pt content, Pt<sub>53</sub>Au<sub>47</sub> and Pt<sub>78</sub>Au<sub>22</sub> exhibited predominantly Pt–Pt bonding, which reflects their more complete Au-core/Pt-shell structures.

The emerging picture of these nanoparticles as containing Pt preferentially located at the surface of Au cores is consistent with real-space imaging of these nanoparticles using atomic resolution HAADF-STEM and elemental imaging using spatially resolved EDX spectroscopy (Fig. 2a–c). To prevent beam damage to these nanoparticles, the electron-beam intensity was minimized during EDX spectroscopy measurements, which resulted in low X-ray counting statistics; nonetheless, there is strong evidence for Au signal that originates mainly from the cores of nanoparticles, with the Pt signal being more diffuse and slightly enhanced at the particle edges. This effect can also be illustrated by comparing the overlay EDX maps of representative particles shown in Fig. 2a–c. It is noteworthy that a similar control over surface structure generally requires two or more sequential steps during the synthesis, as Pt and Au are capable of forming homogeneous alloys<sup>23–26</sup>. The ability to achieve these complex surface morphologies in a single reaction

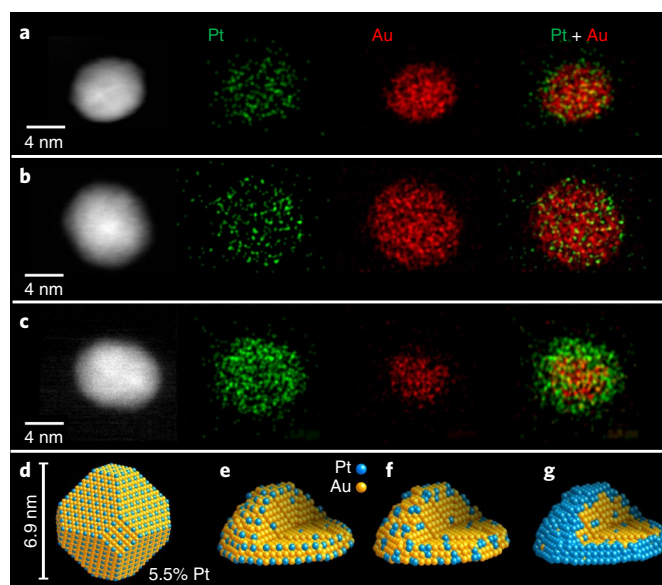


**Fig. 2 | HAADF-STEM images and structural models. a–c**, STEM/EDX mapping images of individual particles from Pt<sub>4</sub>Au<sub>96</sub> (**a**) and Pt<sub>7</sub>Au<sub>93</sub> (**b**) single-atom Pt samples and from a Pt<sub>78</sub>Au<sub>22</sub> core-shell sample (**c**). **d**, Structural model of an ideal, truncated octahedral nanoparticle with an optimal single-atomic-site coverage. Although strictly not representative of the nanoparticles synthesized here, this model provides a reasonable estimate of the upper concentration limit for such single-atom Pt sites. **e–g**, Models that depict the proposed evolution of PtAu surface structures from single-atom Pt sites (**e**) to few-atom Pt clusters (**f**) to a complete Pt shell (**g**) as a result of increased Pt content.

step probably stems from a combination of factors, which include sequential reduction (due to the more negative reduction potential of Au relative to Pt) and preferential coordination of the stabilizing amine ligands to the surface Pt sites rather than to the Au sites<sup>27,28</sup>. The significantly greater adsorption energy of the oleylamine ligand molecules at the surface Pt sites can contribute to the preferential Au-core/Pt-shell structure of the PtAu nanoparticles, as it results in a greater stabilization and limits further deposition of Au atoms, which thereby results in a Pt-enriched surface.

The observation of a Pt-rich surface is consistent with a single-atom Pt surface structure. For an ideal truncated octahedral nanoparticle (Fig. 2d), the maximum surface coverage by single-atom sites (that is, with no co-adjacent Pt atoms) is achieved with a Pt content of 5.5%. Although atomic-scale HAADF-STEM images suggest that the PtAu nanoparticles synthesized here are

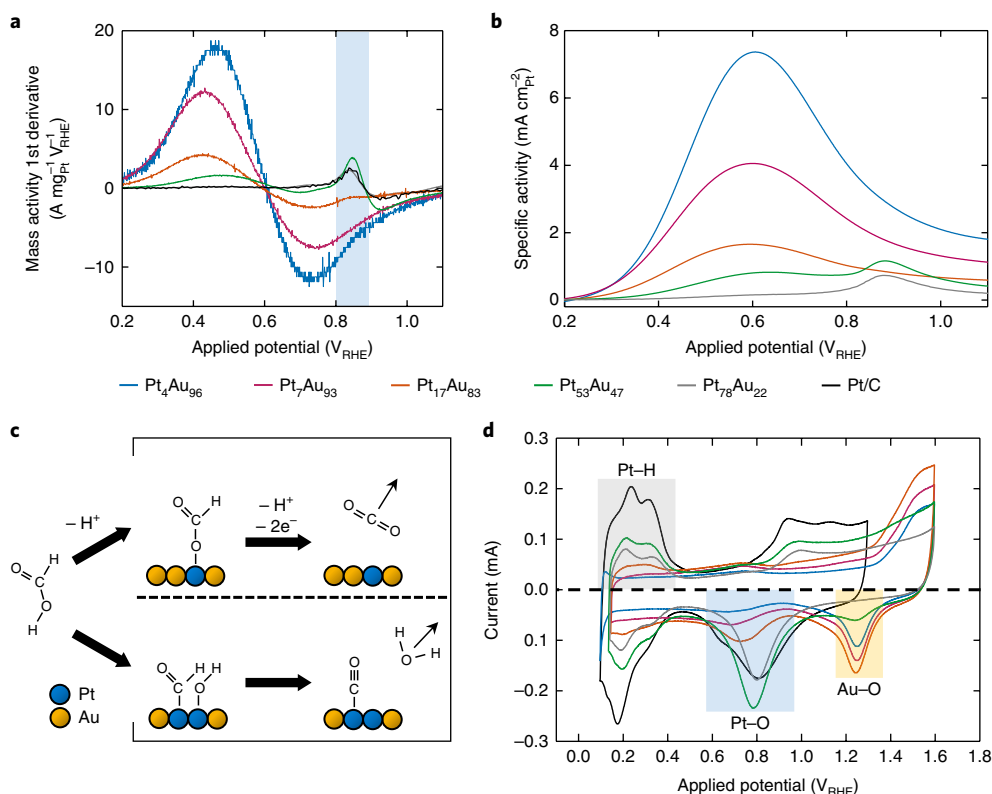


**Fig. 3 | Further electrochemical analysis.** **a**, The first derivative of the Pt mass-normalized FAO voltammograms presented in Fig. 1a. The blue area highlights the sensitivity of the first-derivative peak at  $-0.85 V_{\text{RHE}}$  to the Pt surface structure. **b**, FAO anodic sweep voltammograms obtained from PtAu nanoparticle and commercial Pt/C catalyst samples, as normalized by the ECSA of Pt. These voltammograms were also obtained using a sweep rate of  $10 \text{ mV s}^{-1}$  and an electrolyte that contained  $0.1 \text{ M}$  concentrations of both  $\text{HClO}_4$  and  $\text{HCOOH}$ . **c**, Illustration of the dehydrogenation (top) and dehydration (bottom) mechanisms of the FAO reactions on PtAu surfaces. **d**, Cyclic voltammograms from PtAu nanocatalysts (shown at full amplitude) and commercial Pt nanocatalysts (shown at half amplitude to facilitate the comparison) acquired in  $0.1 \text{ M HClO}_4$  with a sweep rate of  $100 \text{ mV s}^{-1}$ .

predominantly polycrystalline, this single-crystalline estimate serves as a reasonable upper concentration limit at which exclusively single-atom Pt sites are able to exist, and suggests that  $\text{Pt}_4\text{Au}_{96}$  and  $\text{Pt}_7\text{Au}_{93}$  could reasonably exhibit such a surface morphology.

Based on the available information, the PtAu samples can now be categorized in terms of their surface structure: Au with single-atom Pt sites ( $\text{Pt}_7\text{Au}_{93}$  and  $\text{Pt}_4\text{Au}_{96}$ ), Au with single-atom and few-atom Pt sites ( $\text{Pt}_{17}\text{Au}_{83}$ , and Au-core/Pt-shell ( $\text{Pt}_{78}\text{Au}_{22}$  and  $\text{Pt}_{53}\text{Au}_{47}$ ). This gradual change from single-atom to near-complete shell coverage in these PtAu/C nanocatalysts is illustrated in Fig. 2e–g. Additional support for the proposed surface structures of the nanoparticles is given in the detailed analysis of their electrocatalytic performance presented in Fig. 3. The disappearing peak at  $\sim 0.85 V_{\text{RHE}}$  in Fig. 1b is more clearly shown in the first-derivative plots of the Pt mass activity in Fig. 3a. Such a peak intensity was completely absent in both the  $\text{Pt}_7\text{Au}_{93}$  and  $\text{Pt}_4\text{Au}_{96}$  samples (as is more clearly illustrated in Supplementary Fig. 9), and was markedly reduced in  $\text{Pt}_{17}\text{Au}_{83}$ . These electrochemical results offer another piece of evidence for the Pt single-atom structure in  $\text{Pt}_7\text{Au}_{93}$  and  $\text{Pt}_4\text{Au}_{96}$ . As is illustrated in Fig. 3c, the existence of adjacent Pt surface sites will produce a CO poisoning peak in the first-derivative voltammogram, whereas the single-atom Pt geometry of the catalyst surface will encourage carbon dioxide formation via the dehydrogenation mechanism. Moreover, the small CO first-derivative peak for  $\text{Pt}_{17}\text{Au}_{83}$  in Fig. 3a illustrates the existence of some smaller, cluster-like Pt domains in this sample. Figure 3b shows that a similar trend in specific activity is observed when normalizing FAO anodic sweep voltammograms by the electrochemically active surface area (ECSA) of Pt, which indicates again that the observed increase in activity was not simply

due to an increased proportion of Pt surface sites in those samples with a lower Pt content. Both  $\text{Pt}_7\text{Au}_{93}$  and  $\text{Pt}_4\text{Au}_{96}$  exhibited very similar peak intensities when the anodic sweeps were normalized by the combined ECSAs of Pt and Au, which suggests that they shared a similar surface structure in addition to their mutual resistance to CO poisoning. Finally, normalization of electrocatalytic performance by the total metal catalyst mass resulted in a trade-off between the reduced surface poisoning by CO and the number of available Pt catalytic sites (Supplementary Fig. 10).

This structure is experimentally supported by the behaviour of distinct Au–O adlayer formation on the exposed Au surfaces, as revealed by CV measurements under non-catalytic conditions (Fig. 3d). Regions of interest include the positive Pt–H desorption peaks highlighted from about  $0.1$  to  $0.4 V_{\text{RHE}}$ , and the negative Pt–O and Au–O adlayer removal peaks highlighted from  $0.55$  to  $0.95 V_{\text{RHE}}$  and from  $1.15$  to  $1.35 V_{\text{RHE}}$ , respectively. As expected from the relative compositions, the areas of the Pt–O and Au–O adlayer removal peaks revealed a gradual transition from a pure Pt surface in  $\text{Pt}_{78}\text{Au}_{22}$  (indicative of its Au-core/Pt-shell structure) to the predominantly Au surface decorated with Pt in  $\text{Pt}_4\text{Au}_{96}$ . In addition to a steady reduction of the Pt–H peak area, a significant negative shift of the Pt–O adlayer removal peak was observed with decreasing Pt content; this shift reached a maximum of  $\sim 0.1 V_{\text{RHE}}$  in  $\text{Pt}_4\text{Au}_{96}$ , which reveals a markedly strengthened Pt–O adsorption, probably due to the increasingly lowered coordination numbers of Pt atoms in these samples. This observation provides strong evidence for the thorough mixing of Pt and Au at the surface of samples with a low Pt content, which results in a relatively even distribution of Pt across the predominantly Au surface. The less-drastic shift of the Au–O

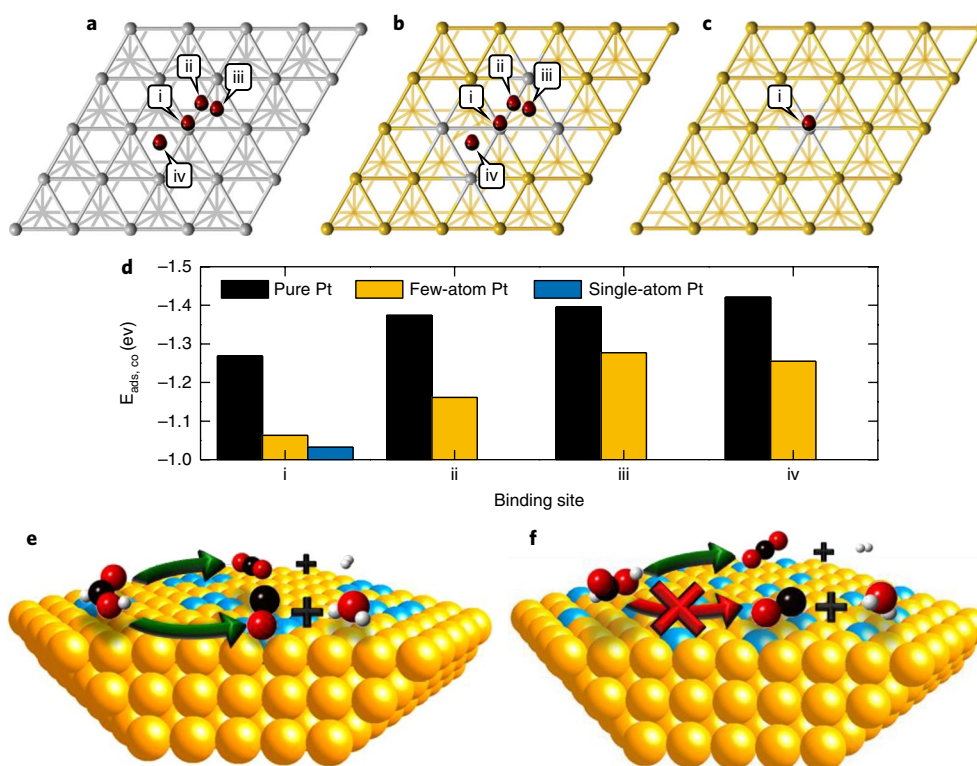


**Fig. 4 | DFT-calculated binding of CO at PtAu surfaces.** **a–c**, Illustration of CO adsorption modes on model (111) lattices of pure **(a)**, few-atom **(b)** and single-atom **(c)** Pt surfaces that shows the apical (i), bridging (ii), hexagonal close-packed hollow (iii) and face-centred cubic hollow (iv) coordination sites. **d**, Calculated adsorption energies for the indicated CO adsorption sites. **e, f**, Predominant FAO reaction pathways on few-atom (or greater) **(e)** and single-atom **(f)** Pt surfaces, which highlights the selectivity achieved via the ensemble effect. Spheres: Au, yellow; C, black; H, white; O, red, Pt, blue.

adlayer desorption peak relative to that of Pt–O can be explained by the fact that any charge transfer effects involve up to nine Au atoms per Pt atom, depending on the relative composition of the sample.

Given that CO poisoning has a drastic impact on the measured activity of Pt-based FAO catalysts, DFT calculations were performed to study the adsorption properties of CO at single-atom, few-atom and pure Pt surfaces (Fig. 4a–c). The (111) surface is selected in our DFT calculations because the (111) sites are the most-abundant surface sites in regular colloidal Au and Pt nanoparticles. Multiple adsorption sites for CO exist at pure and few-atom Pt surfaces (in order of increasing adsorption energy: apical, bridging, hexagonal close-packed hollow and face-centred cubic hollow), whereas only a single site (apical) was found to be significant for the single-atom Pt surface. The results of these calculations indicate that CO adsorption is weakened at all the adsorption sites on both few-atom and single-atom Pt surfaces relative to bulk Pt (Fig. 4d and Supplementary Table 3). Adsorption energies of CO at the apical sites, for example, are reduced from  $-1.268$  eV on bulk Pt to  $-1.063$  and  $-1.032$  eV on few-atom and single-atom surfaces, respectively. This finding is in line with the observed enhancement in FAO activity, rationalized via a weakening of the typically too-strong CO adsorption on Pt (as per the Sabatier Principle)<sup>29,30</sup>. Although this weakened CO adsorption is consistent with the observed activity enhancement, it is generally recognized that the availability of adjacent adsorption sites also makes a significant contribution to FAO activity<sup>7</sup>. Note that the PtAu nanoparticles also show a significant retention of activity, as shown by both the chronoamperometric measurements performed at  $0.55 V_{\text{RHE}}$  and the repeated cycling between  $0.1$  and  $1.1 V_{\text{RHE}}$  (Supplementary Fig. 11). These results further indicate the fairly good stability of the alloy-based single-atom catalysts, with the latter demonstrating that a high activity ( $>70\%$  of the initial value) can be retained even after 1,500 successive rounds of potential cycling.

Although a number of possible pathways exist for the oxidation of formic acid at Pt surfaces, the dehydrogenation and dehydration pathways tend to predominate overall (Fig. 4e)<sup>30</sup>. The former pathway is responsible for the majority of the observed FAO activity of Pt, but the latter is a major concern as it leads to the formation of adsorbed CO species at Pt sites and blocks them from participating in future reaction steps. Due to its large impact on catalytic activity, surface morphology also plays a major role in determining which of these two reaction pathways predominates. Both DFT calculations<sup>31</sup> and experimental evidence<sup>32</sup> support this observation, which indicates that only one Pt adsorption site is required for formic acid dehydrogenation, whereas the indirect dehydration pathway requires a greater number of adjacent atoms. This so-called ‘ensemble effect’ strongly discourages the detrimental indirect reaction to leave the direct dehydrogenation reaction as the primary reaction pathway (Fig. 4f). Thus, the formation of isolated single-atom catalytic sites can be linked to the remarkable activity increases observed in these PtAu nanocatalysts.

Valence band analysis was also performed on the PtAu/C nanocatalyst using both DFT density of states (DOS) calculations and XPS measurements to better understand the electronic effect of alloy formation on catalytic activity. The DFT DOS results in Fig. 5a predict a drastic reduction of intensity near the Fermi level (that is,  $0$  eV) for the single-atomic-site Pt surface relative to the pure Pt surface. Tellingly, in the XPS valence band measurements shown in Fig. 5b–e, the near-Fermi level DOS (that is,  $-2$  to  $0$  eV) is also found to be very sensitive to the local structural environment of Pt. The two samples that bear single-atom Pt sites, Pt<sub>4</sub>Au<sub>96</sub> and Pt<sub>7</sub>Au<sub>93</sub>, show the lowest DOS intensity in the near-Fermi level region, being virtually identical to the pure Au surface. In contrast, a pronounced increase in the DOS intensity near the Fermi level is observed for the few-atom-cluster Pt sample, Pt<sub>17</sub>Au<sub>83</sub>. Finally, when a more complete

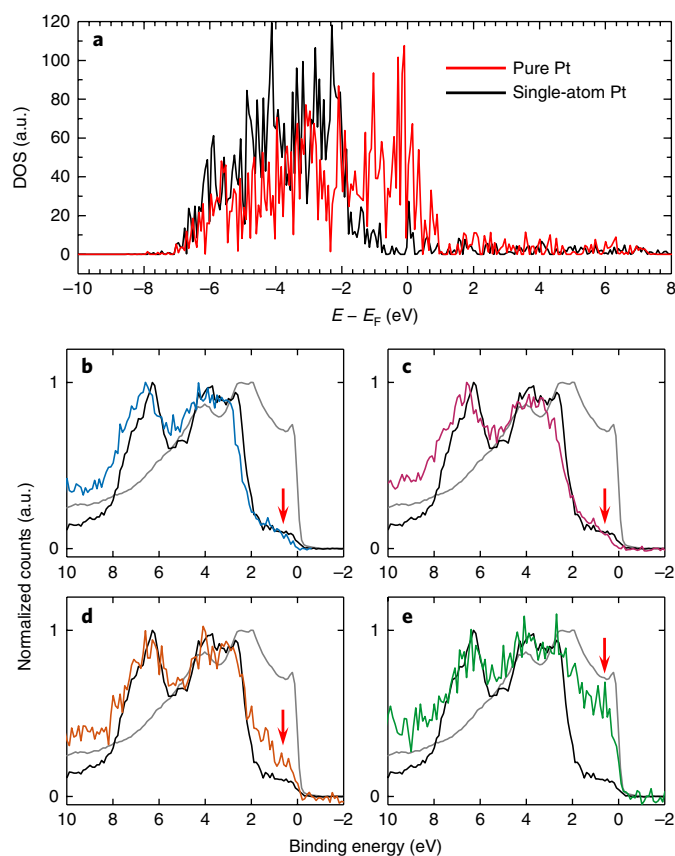


**Fig. 5 | Calculated and experimental DOS.** **a**, Calculated DFT DOS plots that correspond to the pure and single-atom Pt surfaces used to calculate the CO adsorption energies in Fig. 4a–d. **b–e**, XPS valence band spectra of Pt<sub>4</sub>Au<sub>96</sub> (**b**), Pt<sub>7</sub>Au<sub>93</sub> (**c**), Pt<sub>17</sub>Au<sub>83</sub> (**d**) and Pt<sub>53</sub>Au<sub>47</sub> (**e**) samples compared with those of Pt (grey) and Au (black) foil references. The red arrows indicate the near-Fermi level region, wherein samples that contain single-atom Pt sites show a considerable difference to those that contain few-atom cluster and core-shell Pt surfaces.

Pt shell is formed at the Au nanoparticle surface, as in Pt<sub>53</sub>Au<sub>47</sub>, the near-Fermi level DOS becomes higher still and its intensity begins to approach that of the pure Pt surface.

These results indicate that samples that contain larger amounts of Pt demonstrate a much more pronounced Pt character in their valence bands, which results in increased DOS intensities near the Fermi level. For single-atom Pt surfaces, however, no such Pt–Pt bonding exists and the overall DOS is determined by the predominant Au–Au bonding. Thus, the low DOS intensities observed near the Fermi level of single-atom Pt surfaces arise from the large number of Au atoms relative to Pt. When Pt–Pt bonds begin to appear, as occurs in the few-atom Pt clusters of Pt<sub>17</sub>Au<sub>83</sub>, the DOS intensity of the near-Fermi level increases considerably. These results are in good agreement with previous observations that the DOS intensity near the Fermi level is determined primarily by chemical bonding between kindred nearest-neighbour atoms<sup>33</sup>. This means that the identical near-Fermi level DOS intensities observed for Pt<sub>4</sub>Au<sub>96</sub>, Pt<sub>7</sub>Au<sub>93</sub> and the bulk Au reference prove, again, the single-atom Pt structure for these two PtAu nanoparticle samples. Furthermore, the valence band structure of the PtAu nanoparticle samples is also closely linked to their catalytic performance. Due to relativistic effects, the *d* orbitals of Au are higher in energy, and the valence *s* orbital lower, than would typically be expected, which results in a shift of electron density from the former to the latter. As a result, Au atoms are less able to accept  $\sigma$ -donated electrons and engage in

$\pi$  back-donation to adsorbed CO molecules, which weakens the CO adsorption energies on these surfaces, as shown in Fig. 4.

In conclusion, bimetallic PtAu nanoparticles with extraordinary electrocatalytic FAO activity were synthesized using a facile and easily tunable colloidal method. By employing a comprehensive suite of structural characterization techniques, these PtAu nanocatalysts were identified as having distinct Au-core/Pt-shell, few-atom Pt cluster or single-atom Pt surface structures, dictated by their relative elemental compositions. Structural characterization revealed a high surface density of low-coordinate, single-atom Pt sites in Pt<sub>7</sub>Au<sub>93</sub> and Pt<sub>4</sub>Au<sub>96</sub>, which, according to the ensemble effect theory, prevented these catalysts from self-poisoning via CO generation at their surfaces. Thus, the observed orders-of-magnitude increase in Pt mass-normalized FAO activity for the best-performing PtAu nanocatalyst (single-atom Pt<sub>4</sub>Au<sub>96</sub>) relative to the poorest (core-shell Pt<sub>78</sub>Au<sub>22</sub> and commercial Pt) is readily explained in terms of surface structure and alloy bonding. DFT calculations further supported these results by revealing a weakened adsorption of CO to few-atom and single-atom Pt surfaces as a result of both electronic effects that arise from Pt–Au bonding interactions and the formation of discrete single-atom Pt catalytic sites (that is, the ensemble effect). Unlike many other published syntheses, only a single-step colloidal method was required to achieve a high degree of control over the surface structure and alloy bonding, and a very high surface packing density of single-atom catalytic sites up to 7% can be achieved. As a result, the excellent electrocatalytic activity of these PtAu nanoparticles represents remarkable progress in the development of single-atomic-site Pt catalysis with exceptional selectivity that enables the use of highly active Pt to perform reactions typically prohibited by CO poisoning.

### Online content

Any methods, additional references, Nature Research reporting summaries, source data, statements of data availability and associated accession codes are available at <https://doi.org/10.1038/s41563-018-0167-5>.

Received: 12 January 2018; Accepted: 13 August 2018;  
Published online: 24 September 2018

### References

- Chen, A. & Holt-Hindle, P. Platinum-based nanostructured materials: synthesis, properties, and applications. *Chem. Rev.* **110**, 3767–3804 (2010).
- Hunt, S. T. et al. Self-assembly of noble metal monolayers on transition metal carbide nanoparticle catalysts. *Science* **352**, 974–978 (2016).
- Yu, Y., Wang, X. & Lim, K. H. A DFT study on the adsorption of formic acid and its oxidized intermediates on (100) facets of Pt, Au, monolayer and decorated Pt@Au surfaces. *Catal. Lett.* **141**, 1872–1882 (2011).
- Wang, X., He, B., Hu, Z., Zeng, Z. & Han, S. Current advances in precious metal core-shell catalyst design. *Sci. Technol. Adv. Mater.* **15**, 043502 (2014).
- Liu, X., Wang, D. & Li, Y. Synthesis and catalytic properties of bimetallic nanomaterials with various architectures. *Nano Today* **7**, 448–466 (2012).
- Liu, X., Wang, D. & Li, Y. Bimetallic nanocrystals: liquid-phase synthesis and catalytic applications. *Adv. Mater.* **23**, 1044–1060 (2011).
- Jiang, K., Zhang, H.-X., Zou, S. & Cai, W.-B. Electrocatalysis of formic acid on palladium and platinum surfaces: from fundamental mechanisms to fuel cell applications. *Phys. Chem. Chem. Phys.* **16**, 20360–20376 (2014).
- Liu, J. et al. Tackling CO poisoning with single atom alloy catalysts. *J. Am. Chem. Soc.* **138**, 6396–6399 (2016).
- Yuge, K., Koyama, Y., Kuwabara, A. & Tanaka, I. Surface design of alloy protection against CO-poisoning from first principles. *J. Phys. Condens. Matter.* **26**, 355006 (2014).
- Habrioux, A. et al. Structural and electrochemical studies of Au–Pt nanoalloys. *Phys. Chem. Chem. Phys.* **11**, 3573–3579 (2009).
- Ji, X. et al. Nanocrystalline intermetallics on mesoporous carbon for direct formic acid fuel cell anodes. *Nat. Chem.* **2**, 286–293 (2010).
- Zhang, H., Watanabe, T., Okumura, M., Haruta, M. & Toshima, N. Catalytically highly active top gold atom on palladium nanocluster. *Nat. Mater.* **11**, 49–52 (2012).
- Guo, S. et al. Nanocatalyst superior to Pt for oxygen reduction reactions: the case of core/shell Ag(Au)/CuPd nanoparticles. *J. Am. Chem. Soc.* **136**, 15026–15033 (2014).

14. Yang, X.-F. et al. Single-atom catalysts: a new frontier in heterogeneous catalysis. *Acc. Chem. Res.* **46**, 1740–1748 (2013).
15. Qiao, B. et al. Single-atom catalysis of CO oxidation using Pt<sub>1</sub>/FeO<sub>x</sub>. *Nat. Chem.* **3**, 634–641 (2011).
16. Chen, G. et al. Interfacial effects in iron-nickel hydroxide–platinum nanoparticles enhance catalytic oxidation. *Science* **344**, 495–499 (2014).
17. Roy, A. et al. Enhanced catalytic activity of Ag/Rh bimetallic nanomaterial: evidence of an ensemble effect. *J. Phys. Chem. C* **120**, 5457–5467 (2016).
18. Prinz, J. et al. Ensemble effect evidenced by CO adsorption on the 3-fold PdGa surfaces. *J. Phys. Chem. C* **118**, 12260–12265 (2014).
19. Zaera, F., Gellman, J. A. & Somorjai, G. A. Surface science studies of catalysis: classification of reactions. *Acc. Chem. Res.* **19**, 24–31 (1986).
20. Ruff, M., Takehiro, N., Liu, P., Nørskov, J. K. & Behm, R. J. Size-specific chemistry on bimetallic surfaces: a combined experimental and theoretical study. *ChemPhysChem* **8**, 2068–2071 (2007).
21. Sachtler, W. M. H. Chemisorption complexes on alloy surfaces. *Catal. Rev. Sci. Eng.* **14**, 193–210 (1976).
22. Stevanović, S. et al. Insight into the effect of Sn on CO and formic acid oxidation at PtSn catalysts. *J. Phys. Chem. C* **118**, 278–289 (2014).
23. Duchesne, P. N. & Zhang, P. Element-specific analysis of the growth mechanism, local structure, and electronic properties of Pt clusters formed on Ag nanoparticle surfaces. *J. Phys. Chem. C* **118**, 21714–21721 (2014).
24. Yu, Y., Hu, Y., Liu, X., Deng, W. & Wang, X. The study of Pt@Au electrocatalyst based on Cu underpotential deposition and Pt redox replacement. *Electrochim. Acta* **54**, 3092–3097 (2009).
25. Kim, J., Jung, C., Rhee, C. K. & Lim, T. Electrocatalytic oxidation of formic acid and methanol on Pt deposits on Au(111). *Langmuir* **23**, 10831–10836 (2007).
26. Luo, J. et al. Phase properties of carbon-supported gold–platinum nanoparticles with different bimetallic compositions. *Chem. Mater.* **17**, 3086–3091 (2005).
27. Atkins, P. & de Paula, J. *Atkins' Physical Chemistry* 8th edn, 1005–1006 (W.H. Freeman and Company, New York, 2006).
28. Wu, B. & Zheng, N. Surface and interface control of noble metal nanocrystals for catalytic and electrocatalytic applications. *Nano Today* **8**, 168–197 (2013).
29. Bligaard, T. et al. The Brønsted–Evans–Polanyi relation and the volcano curve in heterogeneous catalysis. *J. Catal.* **224**, 206–217 (2004).
30. Zhong, W. & Zhang, D. New insight into the CO formation mechanism during formic acid oxidation on Pt(111). *Catal. Commun.* **29**, 82–86 (2012).
31. Neurock, M., Janik, M. & Wieckowski, A. A first principles comparison of the mechanism and site requirements for the electrocatalytic oxidation of methanol and formic acid over Pt. *Faraday Discuss.* **140**, 363–378 (2009).
32. Cuesta, A., Escudero, M., Lanova, B. & Baltruschat, H. Cyclic voltammetry, FTIRS, and DEMS study of the electrooxidation of carbon monoxide, formic acid, and methanol on cyanide-modified Pt(111) electrodes. *Langmuir* **25**, 6500–6507 (2009).
33. Mason, M. Electronic structure of supported small metal clusters. *Phys. Rev. B* **27**, 748–762 (1983).

## Acknowledgements

P.Z. acknowledges financial support from the NSERC Canada Discovery Grant and P.N.D. was funded by an NSERC CGS scholarship. Financial supports from European COST Action MP0903 'Nanoalloy' (Z.Y.L.) and the US National Science Foundation DMR-1409396 (S.C.) are acknowledged. A.A. and Z.A. acknowledge the financial support by Deanship of Scientific Research, King Saud University. Part of this work was supported by a PCOSS Open Project Grant (Xiamen University) awarded to P.Z. and hosted by N.Z. DFT calculations were sponsored by the U.S. Department of Energy, Office of Science, Office of Basic Energy Sciences, Chemical Sciences, Geosciences, and Biosciences Division and used resources of the National Energy Research Scientific Computing Center, a DOE Office of Science User Facility supported by the Office of Science of the U.S. Department of Energy under contract no. DE-AC02-05CH11231. This research used resources of the Advanced Photon Source, an Office of Science User Facility operated for the US Department of Energy (DOE) Office of Science by Argonne National Laboratory, and was supported by the US DOE under contract no. DE-AC02-06CH11357, and the Canadian Light Source and its funding partners. The Canadian Light Source is supported by the CFI, NSERC, NRC, CIHR, the University of Saskatchewan, the Government of Saskatchewan and Western Economic Diversification Canada. We are also grateful for the assistance of Z. Finfrock (CLS@APS) and Y. Hu (SXRMB@CLS) for synchrotron technical support, and L. Leonardo for the collection of additional EDX mapping in the JEOL-York Nanocenter using JEM-2200FS Cs-corrected (S)TEM operating at 200 keV.

## Author contributions

P.N.D. synthesized all the samples, conducted the XAS experiments and analysis, performed some of the electrochemical and TEM studies, and wrote the manuscript. P.Z. designed the project, coordinated the process of the work and supervised P.N.D. to conduct this research. Z.Y.L. and J.Y. performed the HAADF-STEM measurements and image analysis. C.P.D. performed the electrochemical experiments under the supervision of S.C. V.F. conducted the DFT calculations under the supervision of D.J. X.Z. contributed to the TEM measurements under the supervision of N.Z. A.A. and Z.A. also contributed to part of the TEM measurements. T.R. performed some of the XPS measurements at the Canadian Light Source.

## Competing interests

The authors declare no competing financial interests.

## Additional information

**Supplementary information** is available for this paper at <https://doi.org/10.1038/s41563-018-0167-5>.

**Reprints and permissions information** is available at [www.nature.com/reprints](http://www.nature.com/reprints).

**Correspondence and requests for materials** should be addressed to P.Z.

**Publisher's note:** Springer Nature remains neutral with regard to jurisdictional claims in published maps and institutional affiliations.

## Methods

**Materials.** Dihydrogen hexachloroplatinate ( $\text{H}_2\text{PtCl}_6 \cdot 6\text{H}_2\text{O}$ , 99.9%), hydrogen tetrachloroaurate ( $\text{HAuCl}_4 \cdot 3\text{H}_2\text{O}$ , 99.9%), ethylene glycol (99+%) and a HiSPEC 3000 carbon-supported Pt catalyst (Pt/C,  $\leq 500$  ppm impurities) were purchased from Alfa Aesar. Oleylamine (OAm) (C18-content 80–90%) and formic acid (HCOOH, 99%) were purchased from Acros Organics. Vulcan XC-72 carbon powder was purchased from Cabot. Nafion 117 Solution (Nafion, 5%) and *n*-butylamine ( $\text{BuNH}_2$ , 99.5%) were purchased from Sigma Aldrich. Perchloric acid ( $\text{HClO}_4$ , 70%) was purchased from Fisher Scientific. Ethanol used in the CV experiments (EtOH, 96%) was purchased from J.T. Baker. All the reagents and solvents were used as received, without further purification.

**Synthesis of PtAu nanoparticles.** PtAu nanoparticles were prepared from stock solutions of Pt and Au chloride precursor salts, with nominal compositions of 10, 25, 50 and 75 atom% Pt being selected by controlling the ratio of precursors used. In a typical synthesis, 72.5 mg of  $\text{H}_2\text{PtCl}_6 \cdot 6\text{H}_2\text{O}$  and 55.1 mg of  $\text{HAuCl}_4 \cdot 3\text{H}_2\text{O}$  were each dissolved in 70 ml of OAm through a combination of ultrasonication and manual mixing to obtain metal precursor stock solutions. Appropriate volumes of these Pt and Au stock solutions (prepared in OAm) were then added to a 100 ml round-bottomed flask to give the desired Pt-to-Au ratio with a total volume of 20 ml. An additional 20 ml of ethylene glycol was then added with vigorous mixing using a magnetic stirrer. The resulting mixture was subsequently bubbled with  $\text{N}_2(\text{g})$  for several minutes in order to remove dissolved  $\text{O}_2(\text{g})$  from solution. Each mixture was then placed in a 180 °C oil bath, sealed, and allowed to react for 1 h. Once the reaction was complete, the flask was removed from the heat and allowed to cool to room temperature while still sealed under a  $\text{N}_2$  atmosphere. Due to the large excess of reducing agents employed in this reaction (OAm and ethylene glycol, also functioning as solvents), all the  $\text{Pt}^{4+}$  and  $\text{Au}^{3+}$  species can reasonably be assumed to have been reduced to a zero-valent state. To purify the product nanoparticles, each sample was divided amongst several 30 ml polypropylene centrifuge tubes. The nanoparticles were precipitated via the addition of two to three volume equivalents of EtOH, and then isolated by centrifuging the resulting suspension (at 6,000 revolutions per minute (r.p.m.) for 5 min) and decanting the supernatant. The precipitated nanoparticles were then redispersed in hexanes via brief ultrasonication and shaking before being again precipitated and centrifuged. After this second centrifugation cycle, the purified nanoparticles were redispersed in hexanes and centrifuged once more to remove any insoluble material.

**Deposition of PtAu nanoparticles onto XC-72 carbon powder.** After purification, the nanoparticle samples were deposited onto an XC-72 carbon powder support material via ligand-exchange-induced destabilization. A nanoparticle loading of 20 wt% (by total mass of Pt and Au) was selected to allow for a better comparison with the commercial Pt/C catalyst (HiSPEC 3000, 20 wt% Pt) used as a reference material for electrocatalytic testing. For each sample, four mass equivalents of XC-72 powder (assuming a theoretical yield of 100% for each nanoparticle sample) were added to 15 ml of  $\text{BuNH}_2$  and thoroughly dispersed via ultrasonication. Each purified nanoparticle sample was then precipitated using EtOH and isolated via centrifugation and decantation. The isolated nanoparticle material was redispersed and extracted from the centrifuge tube using ultrasonication and successive aliquots of the previously prepared XC-72/ $\text{BuNH}_2$  suspension. This final mixture was then allowed to stir magnetically for 24 h to allow the ligand exchange and nanoparticle deposition to occur gradually. Finally, the postdeposition PtAu nanoparticle materials were isolated once more via EtOH addition and centrifugation (at 12,000 r.p.m. for 20 min) and allowed to dry in air.

**TEM.** Bright-field TEM imaging of the samples was performed both prior to and after deposition onto the XC-72 carbon support. In preparation for the analysis, each sample was dispersed in  $\sim 200$   $\mu\text{l}$  of EtOH via sonication and drop cast onto Formvar-coated copper TEM grids. Unsupported PtAu nanoparticle samples were imaged using a JEOL JEM-2100F transmission electron microscope operated at a 200 kV accelerating voltage. PtAu nanoparticle samples supported on XC-72 carbon powder were imaged using a Tecnai F-30 transmission electron microscope operated at a 300 kV accelerating voltage. Size distributions and mean particle diameters of the nanoparticles were measured and calculated using MacBiophotonics ImageJ software<sup>34</sup> and several representative images from each sample. HAADF and EDX mapping measurements were performed at the University of Birmingham (UK) using a JEOL 2100F scanning transmission electron microscope with a CEOS aberration corrector. A JEOL annular dark-field detector was used for the HAADF imaging and a Bruker XFlash 4030 silicon drift detector was used for the EDX mapping of the PtAu nanoparticle samples. During the EDX mapping, the HAADF-STEM images were monitored to check for possible beam-induced structure changes of the atomic structure. The EDX data presented are from only those nanoparticles that did not show any visible structural changes.

**XAS.** XAS measurements were performed using the Sector 20-BM beamline of the Advanced Photon Source at Argonne National Laboratory (Argonne, IL). The end station was equipped with a double-crystal Si(111) monochromator for wavelength selection, which was detuned to 80% to help reject higher

harmonics of the desired energy; a toroidal focusing mirror was also employed to further enhance harmonic rejection. Gas-ionization detectors were used to measure the absorption spectra of Pt and Au foil reference materials; however, data acquisition from the bimetallic nanoparticles was complicated by overlap between the spectra obtained at the Pt and Au  $L_2$  edges (which occur at 11,562.76 eV and 11,919.70 eV, respectively<sup>35</sup>). This challenge was addressed by employing a 12-element Ge fluorescence detector to collect data from the bimetallic PtAu nanoparticles. Although there also exists overlap between the Pt and Au  $L_{\alpha}$  emission peaks centred at 9,442.3 eV and 9,713.3 eV, respectively<sup>36</sup>, nearly all of the interfering signal could be filtered out by excluding the overlapping energy region between the two (as depicted in Supplementary Fig. 12). Although excluding this region also resulted in a reduction of the fluorescence intensity, the loss was largely offset by the greater sensitivity of the fluorescence detector relative to standard absorption detectors. As a result, usable spectra were obtained for all the samples through the use of this method. To compensate for the greater amount of noise present in the fluorescence data, PtAu nanoparticle samples were held at  $90 \pm 1$  K during measurements to enhance the EXAFS signal intensity by suppressing thermal vibrations in the material. Full details regarding the data ranges (*k* range and *R* range) used to obtain and fit the FT-EXAFS spectra are presented in Supplementary Table 4. Data processing and fitting were performed using WinXAS<sup>37</sup> and Analyzer v0.1 software, with scattering paths generated by FEFF8<sup>38</sup>.  $S_0^2$  values for Pt and Au (both equal to 0.93) were obtained by fitting a metallic reference foil of same element. A bulk, homogeneous PtAu alloy structural model was used to calculate the Pt–M and Au–M scattering paths used in the FT-EXAFS fitting. A single metal–metal scattering path was used in fitting the FT-EXAFS data because insufficient degrees of freedom were available to include separate Pt and Au scattering paths; the Pt–M and Au–M fitting values reported herein thus represent averages of the Pt–Pt/Pt–Au and Au–Au/Au–Pt contributions.

**XPS.** XPS measurements were performed at the Canadian Light Source in Saskatoon, Canada, using an excitation energy of 3,000 eV at the SXRMB beamline and an excitation energy of 300 eV at the SGM beamline. PtAu/C nanocatalyst samples were prepared by spreading the powder onto conductive, double-sided carbon tape, which was then affixed to a copper sample holder. Many scans of each sample were averaged together to obtain higher signal-to-noise ratios. Relative PtAu compositions were determined from the peak areas obtained by fitting the Pt and Au 4f peaks using the  $\text{Au}^0/\text{Au}^+$  and  $\text{Pt}^0/\text{Pt}^{2+}$  contributions in conjunction with empirically derived atomic sensitivity factors<sup>39</sup>. Splitting between  $4f_{5/2}$  and  $4f_{7/2}$  peaks was set based on data obtained from the NIST X-ray Photoelectron Spectroscopy Database<sup>40</sup>. Full-width at half-maximum values for the  $4f_{5/2}$  and  $4f_{7/2}$  peaks within each contribution were correlated to be equal and the relative area ratios were correlated such that  $\text{area}(4f_{7/2}) : \text{area}(4f_{5/2}) = 4:3$ . XPS valence band spectra were collected using an excitation energy of 3,000 eV and normalized by setting the valence band maximum equal to unity.

**CV.** CV was performed using a CHI 710 electrochemical work station with a three-electrode set-up, which included a polished glassy carbon working electrode (rotating disc electrode), a Ag/AgCl reference electrode and a Pt sheet counter electrode. A solution of 0.1 M perchloric acid was used as the supporting electrolyte, with the addition of 0.1 M formic acid during the FAO activity measurements. Catalyst ‘ink’ suspensions were prepared by dispersing the carbon-supported PtAu material in EtOH via ultrasonication to obtain a final catalyst concentration of 1  $\mu\text{g} \mu\text{l}^{-1}$ . A volume of the Nafion solution equal to 1% the volume of the added EtOH was then added and sonicated for a further 15 min to complete the preparation. For oxygen reduction reaction, testing, 20  $\mu\text{l}$  of the catalyst ink were drop cast onto the glassy carbon electrode surface and allowed to dry completely. A 3  $\mu\text{l}$  volume of a diluted Nafion solution (20% v/v in EtOH) was then deposited onto the dried catalyst layer to help improve its physical stability and electrical conductivity. The electrode surface was allowed to dry completely prior to electrochemical testing. After purging the electrolyte solution with ultrahigh purity  $\text{N}_2$ , CV measurements were performed. Pt ECSAs were calculated from the integrated region beneath the hydrogen-desorption peaks in each voltammogram, whereas Au ECSAs were estimated from the integrated area of the Au–O adlayer removal peak.

**DFT calculations.** DFT calculations were performed using Vienna ab initio package software. The revised Perdew–Burke–Erzerhof (RPBE) form of the generalized-gradient approximation was chosen for the electron exchange and correlation to correct for the overbinding of small molecules at the transition metal surfaces observed using the standard PBE approach. Although DFT–RPBE tends to overstabilize the hollow and bridge sites over the top site for CO adsorption on Pt(111), the adsorption energies on these sites are quite close (within 0.10 eV) and in good agreement with the experimental value<sup>41</sup>. The electron–core interaction was described using the projector-augmented wave method. A kinetic energy cutoff of 450 eV was used for the planewaves, and

the Brillouin zone was sampled using a  $3 \times 3 \times 1$  Monkhorst–Pack scheme. The surface model slab was created using a  $4 \times 4$  supercell of the Pt/Au unit cell, with four atomic layers and a 15 Å unit cell. Adsorption energies were calculated using the equation:

$$E_{\text{ads}} = E_{\text{surface+adsorbate}} - (E_{\text{surface}} + E_{\text{adsorbate}})$$

wherein the energy of the adsorbate,  $E_{\text{adsorbate}}$ , was computed by placing the CO adsorbate molecule in a 10 Å wide cubic cell vacuum to prevent intermolecular interactions that resulting from the periodic boundary conditions.

### Data availability

The data supporting the results of this work are available from the authors on reasonable request.

### References

- Schneider, C. A., Rasband, W. S. & Eliceiri, K. W. NIH Image to ImageJ: 25 years of image analysis. *Nat. Methods* **9**, 671–675 (2012).
- Kraft, S., Stümpel, J., Becker, P. & Kuetgens, U. High resolution X-ray absorption spectroscopy with absolute energy calibration for the determination of absorption edge energies. *Rev. Sci. Instrum.* **67**, 681–687 (1996).
- Bearden, J. A. X-ray wavelengths. *Rev. Mod. Phys.* **39**, 78–124 (1967).
- Ressler, T. WinXAS: A program for X-ray absorption spectroscopy data analysis under MS-Windows. *J. Synchrotron. Radiat.* **5**, 118–122 (1998).
- Ankudinov, A. L., Ravel, B., Rehr, J. J. & Conradson, S. D. Real-space multiple-scattering calculation and interpretation of X-ray-absorption near-edge structure. *Phys. Rev. B* **58**, 7565–7576 (1998).
- Wagner, C. D. in *Practical Surface Analysis* (eds Briggs, D. & Seah, M. P.) 635–638 (Wiley, Hoboken, 1990).
- Naumkin, A. V., Kraut-Vass, A., Gaarenstroom, S. W. & Powell, C. J. *NIST X-ray Photoelectron Spectroscopy Database* (NIST, 2012); <http://srdata.nist.gov/xps/>
- Luo, S., Zhao, Y. & Truhlar, D. G. Improved CO adsorption energies, site preferences, and surface formation energies from a meta-generalized gradient approximation exchange–correlation functional, M06-L. *J. Phys. Chem. Lett.* **3**, 2975–2979 (2012).